Compressibility effects on drag reduction by spanwise traveling transversal surface waves in turbulent boundary layers

Xiao Shao [1,*] Marian Albers [1] Matthias Meinke [1] and Wolfgang Schröder [1,2]
[1] *Chair of Fluid Mechanics and Institute of Aerodynamics, RWTH Aachen University, Wüllnerstrasse 5a, 52062 Aachen, Germany*
[2] *JARA Center for Simulation and Data Science, RWTH Aachen University, Templergraben 55, 52056 Aachen, Germany*

(Received 3 February 2025; accepted 25 August 2025; published 23 September 2025)

The effect of compressibility on drag reduction (DR) by spanwise traveling transversal surface waves (STTSW) is investigated in turbulent boundary layer (TBL) flow over a flat plate. Wall-resolved simulations are performed at Mach numbers $M_1 = 0.2$ and $M_2 = 0.7$ over a range of actuation parameters, i.e., wavelength, period, and amplitude. The results based on 36 cases simulated for each Mach number show that DR is more pronounced at higher Mach numbers with a maximum reduction of 19.2% at $M_1 = 0.2$ compared to 27.5% at $M_2 = 0.7$ for identical actuation parameters. This enhanced DR at $M_2 = 0.7$ is mainly due to the formation of spanwise shock waves at higher phase velocities. These spanwise shock waves are generated by the actuated wall deformation that redistributes the pressure field. Upstream of the shock, in the supersonic flow region, the development of streamwise vortices is weakened, resulting in reduced turbulent mixing and dissipation. Downstream of the shock, the turbulent structures are reorganized due to the compression wave leading to locally high wall-shear stress. Integrating the wall-shear stress distribution over the complete surface wave shows that the spanwise shock waves cause significant friction drag reduction. However, the pressure variations upstream and downstream of the shock wave require an increased actuation power, which results in negative net power saving at $M_2 = 0.7$.

DOI: 10.1103/2882-bszw

I. INTRODUCTION

The wall-shear stress in turbulent boundary layers contributes to the overall drag of slender bodies moving through fluids. Friction drag accounts for approximately 50% of the total aerodynamic drag [1]. In turbulent flows, intense and rapid energy exchange causes the entrainment of high-momentum fluid from the outer layers into the near-wall region, thereby creating high shear flow near the wall and thus significant friction drag. For aircraft, a 1% reduction in friction drag can lead to 0.75% reduction in fuel burn during long-distance flights. Therefore, it is essential to decrease the wall-shear stress to achieve energy savings and thereby to lower fuel consumption and pollutant emissions.

*Contact author: x.shao@aia.rwth-aachen.de

Published by the American Physical Society under the terms of the Creative Commons Attribution 4.0 International license. Further distribution of this work must maintain attribution to the author(s) and the published article's title, journal citation, and DOI.

Various drag reduction (DR) techniques have been explored, including passive methods such as riblets and active methods such as wall oscillation, blowing, and suction [2]. Among these, spanwise in-plane wall oscillations, first studied by Jung *et al.* [3], have shown significant potential in reducing drag by modifying near-wall turbulence structures. This concept was later extended to in-plane spanwise traveling waves [4–6] and spanwise traveling transversal waves with sinusoidal deformed walls [7–11]. The effectiveness of these near-wall transverse forcing methods has been thoroughly reviewed by Ricco *et al.* [1] and Fukagata *et al.* [12]. Both studies emphasize the role of the Stokes layer in drag reduction. In spanwise traveling transversal surface waves (STTSW), the wall deformation is achieved by imposing a sinusoidal displacement in the wall-normal direction, which induces velocities in the wall normal and the spanwise direction. This approach contrasts with in-plane spanwise traveling waves, which directly influence only the spanwise velocity component.

Research concerning STTSW has advanced significantly over the past decade. Initially, numerical studies focused on understanding the basic mechanisms of friction drag reduction, which is caused by the effective disruption of the formation and persistence of near-wall vortical structures [7,8]. Subsequent work by Albers *et al.* [9] extended these findings by systematically exploring a broad range of actuation parameters to optimize both drag reduction (DR) and net power saving (NPS). Their studies demonstrated that under certain conditions drag reduction of up to 26% could be achieved. NPS values were generally below 10% and were observed for actuation settings different from those for maximum DR. In other words, there is a tradeoff between achieving high drag reduction and maintaining energy efficiency. Recent investigations by Mäteling *et al.* [11] and Lagemann *et al.* [13] have significantly advanced the understanding of the drag reduction mechanisms by STTSW revealing their sustained efficacy even at moderate Reynolds numbers. At lower Reynolds numbers, friction drag reduction by STTSW is achieved through the deformation and breakup of quasistreamwise vortices. At a higher Reynolds number, a secondary mechanism involving inner-outer layer interactions becomes dominant which balances outer-layer sweeps and maintains drag reduction. This enables consistent drag reduction of up to 26.5% at $\mathrm{Re}_\tau = 1525$ [13].

While the benefits of STTSW in incompressible flows have been well documented, the impact of compressibility in higher Mach number flows, which are crucial in aeronautical applications, has received limited attention in drag reduction studies. The influence of compressibility on drag reduction via spanwise forcing has been predominantly explored through in-plane wall actuation. Yao and Hussain [14] conducted a comprehensive study on compressibility effects in spanwise wall oscillations, examining plane channel flows at Mach numbers $M = 0.3, 0.8$, and 1.5. They observed that drag reduction increased with Mach number up to 47.1% at $M = 1.5$. More recently, Ruby and Foysi [15] confirmed the beneficial effect of compressibility on DR and NPS. They obtained maximum DR at $M = 3$. Gattere *et al.* [16] showed that compressibility significantly enhances the DR effect of streamwise traveling waves particularly at lower frequencies and wave number. Their findings underscore the importance of considering compressibility in the design of flow control strategies since it can lead to substantial improvements in both drag reduction and energy efficiency. In the present study, the impact of compressibility on friction drag reduction in turbulent boundary layers is investigated in detail for spanwise traveling transversal surface waves (STTSW).

The paper is structured as follows. Section II details the numerical setup, including the governing equations, solution methods, and the parameters defining the flow fields. The methodology for quantifying drag reduction and net power saving is also outlined, along with the application of a triple decomposition to separate mean, coherent, and stochastic components of the compressible flow. Section III presents the results, focusing on the evaluation of DR and NPS across various actuation parameters. A detailed analysis is presented on how spanwise shock waves develop, how spanwise shock waves influence turbulence structures, how the turbulent kinetic energy is redistributed, and how the skin friction components are modified. Finally, the key findings on the implications of compressibility for drag reduction are summarized in Sec. IV.

II. NUMERICAL SETUP AND POSTPROCESSING

A. Governing equations and solution method

Turbulence scale-resolving numerical simulations for actively controlled turbulent boundary layer flow are conducted by approximately solving the Navier-Stokes equations using the finite volume (FV) method of the open source in-house multiphysics flow solver m-AIA (multiphysics Aerodynamisches Institute Aachen) [17]. The Navier-Stokes equations for three-dimensional unsteady compressible flow read in integral form

$$\frac{\partial}{\partial t}\int_{\Omega}\mathbf{Q}\,\mathrm{d}\Omega+\oint_{\partial\Omega}\mathbf{H}(\mathbf{Q})\cdot\mathbf{n}\,\mathrm{d}S=\int_{\Omega}\mathbf{F}_{\Omega}\,\mathrm{d}\Omega, \tag{1}$$

where $\mathbf{Q}^{\top}=(\rho,\quad \rho\mathbf{u},\quad \rho E)$ is the vector of conservative variables. The quantity $\mathbf{F}_{\Omega}$ presents the volume force and $\mathbf{H}(\mathbf{Q})$ is the flux vector consisting of the inviscid $\mathbf{H}_{\mathrm{inv}}(\mathbf{Q})$ and viscous fluxes $\mathbf{H}_{\mathrm{vis}}(\mathbf{Q})$:

$$\mathbf{H}(\mathbf{Q})=\mathbf{H}_{\mathrm{inv}}(\mathbf{Q})-\mathbf{H}_{\mathrm{vis}}(\mathbf{Q})=\begin{pmatrix}\rho\mathbf{u}\\ \rho\mathbf{u}\mathbf{u}^{\top}+p\\ \mathbf{u}(\rho E+p)\end{pmatrix}+\frac{1}{\mathrm{Re}_0}\begin{pmatrix}0\\ \bar{\bar{\boldsymbol{\tau}}}\\ \bar{\bar{\boldsymbol{\tau}}}\mathbf{u}+\mathbf{q}\end{pmatrix} \tag{2}$$

with the velocity vector $\mathbf{u}^{\top}=(u,\quad v,\quad w)$. Denoting the dimensional variable by an underline and the state at rest by the subscript 0 the dimensionless density, velocity, pressure, and energy are $\rho=\underline{\rho}/\underline{\rho}_0$, $\mathbf{u}=\underline{\mathbf{u}}/\underline{a}_0$, and $p=\underline{p}/(\underline{\rho}_0\underline{a}_0^2)$, and $E=\underline{E}/\underline{a}_0^2$. The Reynolds number based on the speed of sound at rest is $\mathrm{Re}_0=\underline{\rho}_0\underline{a}_0\underline{L}_{\mathrm{ref}}/\underline{\mu}_0$, where $\underline{L}_{\mathrm{ref}}$ is the reference length. Sutherland's law is used to compute the viscosity μ. The system of equations is closed by assuming a Newtonian fluid and an ideal gas. The stress tensor $\bar{\bar{\boldsymbol{\tau}}}=-2\mu\bar{\bar{\boldsymbol{S}}}+\frac{2}{3}\mu(\boldsymbol{\nabla}\cdot\mathbf{u})\bar{\bar{\mathbf{I}}}$, where $\bar{\bar{\boldsymbol{S}}}=\frac{1}{2}[\boldsymbol{\nabla}\cdot\mathbf{u}+(\boldsymbol{\nabla}\cdot\mathbf{u})^{\top}]$ is the rate of strain tensor and $\bar{\bar{\mathbf{I}}}$ is the identity matrix. The heat flux is expressed by Fourier's law $\mathbf{q}=-k\boldsymbol{\nabla}T$, where $k=c_p\mu/\mathrm{Pr}$ is the thermal conductivity. T is the static temperature, the specific heat capacity at constant pressure is $c_p=\gamma R/(\gamma-1)$ with the ratio of specific heats $\gamma=1.4$, and $\mathrm{Pr}=0.72$ is the Prandtl number for an ideal gas.

The discretization of the inviscid terms $\mathbf{H}_{\mathrm{inv}}$ consists of a mixed centered-upwind AUSM (advective upstream splitting method) scheme at second-order accuracy [18]. The cell-surface values of the flow quantities are reconstructed from the surrounding cell-center values using a monotone upstream scheme for conservation Laws (MUSCL) type strategy. The viscous terms $\mathbf{H}_{\mathrm{vis}}$ are discretized using a modified cell-vertex scheme at second-order accuracy [19]. The temporal integration is based on a second-order explicit five-stage Runge-Kutta method.

Equations (1) are solved for a flat plate flow in a moving reference frame using an arbitrary Lagrangian-Eulerian formulation [20] of the conservation equations. The flow domain is discretized using a structured body fitted mesh. The Cartesian coordinates x, y, and z representing the streamwise, wall-normal, and spanwise directions are defined in Fig. 1. Periodic boundary conditions are implemented in the spanwise direction. The reformulated synthetic turbulence generation (RSTG) method by Roidl *et al.* [21] is imposed at the inflow boundary to generate a fully developed turbulent boundary layer. A characteristic outflow boundary condition is used for the upper free stream boundary and the outflow plane. The trigonometric function

$$y|_{\mathrm{wall}}(x,z,t)=g(x)A\cos\left(\frac{2\pi}{\lambda}(z-ct)\right) \tag{3}$$

defines the wall-normal motion by the wall boundary condition. The quantity A is the wave amplitude, λ is the streamwise wavelength, T is the period, and c is the phase speed which describes the spanwise traveling speed determined by λ/T. $g(x)$ are step functions to manage a gradual spatial implementation and decay of the actuation in the x direction. The configuration consists of a nonactuated region ($0<x/\theta<50$), a transition region ($50<x/\theta<125$) to ensure a smooth surface transition from the flat plate to the wavy surface for all actuation cases, a fully actuated

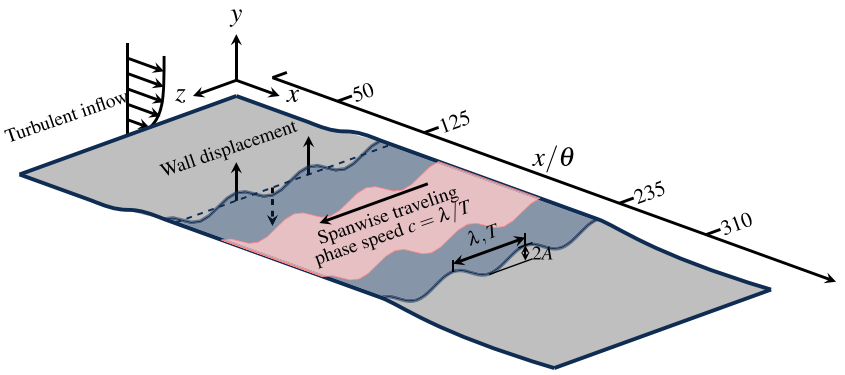


FIG. 1. Schematic of the spanwise traveling transversal surface wave configuration. The wall deformation is imposed in the spanwise direction z as a traveling wave characterized by phase speed $c = \lambda/T$, wavelength λ, and amplitude A. The dark blue region ($125 < x/\theta < 235$) denotes the fully actuated zone. Drag reduction and net power saving are calculated over the red-shaded integration window ($155 < x/\theta < 205$), which remains fixed across all actuation cases.

region ($125 < x/\theta < 235$), and finally a transition to a nonactuated region ($235 < x/\theta < 310$). The momentum thickness θ at $x = 165$ of the nonactuated reference case is equal 1. It is used as reference length for the development of turbulent boundary layers.

The numerical method has been thoroughly validated and proven suitable for the current scenario by numerous analyses of actuated flat plate TBL flows [9,11], actuated turbulent airfoil flows [10], and shock-wave/boundary-layer interactions [22].

B. Simulation cases

Two Mach numbers $M_1 = 0.2$ and $M_2 = 0.7$ are considered to investigate the effect of compressibility on DR and NPS. The Reynolds number based on the momentum thickness of the reference case is $\mathrm{Re}_\theta = \theta_{x_1} u_\infty/\nu = 1000$. The domain sizes are defined by $L_x/\theta = 361$, $L_y/\theta = 101$, and $L_z/\theta = 21.65$, 32.47, 43.30, 54.19, and 64.94. Structured body-fitted curvilinear meshes are used to discretize the physical domain. The grid resolution is $\Delta_x^+ \times \Delta_z^+ \approx 10.0 \times 4.0$, and $\Delta_y^+|_{\mathrm{wall}} \approx 1.0$ with gradual coarsening in the y coordinate yielding a maximum value of $\Delta_y^+ < 16.0$ in the outer region of the boundary layer. The near-wall grid resolution is that of a direct numerical simulation (DNS) to ensure an accurate solution for the impact of wall actuation on turbulent structures. Grid convergence studies were performed in our previous work on STTSW at $M = 0.1$ and $\mathrm{Re}_\theta = 1000$ [9]. The standard resolution with $(\Delta y^+|_{\mathrm{wall}}, \Delta z^+) = (1.0, 4.0)$ yielded drag reduction results deviating by less than 0.01% from the fine-grid solution based on a (0.7, 2.0) mesh resolution. Therefore, the standard mesh is used for the current investigation. The grid resolution validation for $M = 0.7$ is addressed in [23].

The actuation parameter range defined by λ^+, T^+, A^+ in inner scaling based on the friction velocity u_τ, and the kinematic viscosity ν at x_1 using the previous incompressible cases [9] is given in Table I. It is covered by a near-random space-filling sampling method, i.e., Latin hypercube sampling (LHS). To be more precise, 72 cases are performed for $M_1 = 0.2$ and $M_2 = 0.7$.

TABLE I. Dimensionless actuation parameters for wavelength λ^+, time period T^+, and amplitude A^+.

M	λ^+	T^+	A^+
0.2	{1000, 1500, 2000, 2500, 3000}	[70, 160]	[10, 79]
0.7	{1000, 1500, 2000, 2500, 3000}	[70, 160]	[10, 79]

C. Triple decomposition

Turbulent flows exhibit a repeating pattern when subjected to external periodic forcing such as STTSW. The use of triple decomposition allows the separation of velocity and pressure fields into components representing mean, coherent, and stochastic motions [24]. The decomposition for the incompressible turbulent flow defined by the standard Reynolds average reads

$$f = \langle f \rangle(x, y, z) + f''(x, y, z, t) = \bar{f}(x, y) + \tilde{f}(x, y, z) + f''(x, y, z, t), \tag{4}$$

where $\langle f \rangle$ is the phase average of an arbitrary flow variable f combining the temporal and phase-corrected averages. A spatial average of $\langle f \rangle$ in the z direction yields the ensemble mean variable $\bar{f}$. The periodic fluctuations are then computed by $\tilde{f} = \langle f \rangle - \bar{f}$ and the stochastic fluctuations by $f'' = f - \langle f \rangle$.

When it comes to compressible turbulent flow, mass-weighted time averaging is more suitable compared to conventional time averaging. An instantaneous variable via decomposition combined with Favre averaging [25] can be expressed as

$$f = \hat{f} + f''' = \hat{\bar{f}} + \hat{\tilde{f}} + f''', \tag{5}$$

where $\hat{f}$ is the phase Favre averaging with stochastic fluctuations defined as

$$\hat{f} = \langle \rho f \rangle / \langle \rho \rangle. \tag{6}$$

The quantities $\hat{\bar{f}}$ and $\hat{\tilde{f}}$ represent the ensemble mean variable and periodic fluctuation with Favre averaging. The stress tensor with Favre averaging can be written as

$$\widehat{f'''f'''} = \widehat{ff} - \hat{f}\hat{f}. \tag{7}$$

The aditional overbar for this stress tensor, e.g., $\overline{\widehat{f'''f'''}}$, denotes a spanwise averaged variable. Unless specified otherwise, all wall-normal and spanwise distributions are computed at the streamwise location $x/\theta = 180$, i.e., in the center of the fully developed actuated region.

D. Definition of drag reduction and net power saving

The efficiency of the actuation is evaluated based on the drag coefficient $c_{d,x,\mathrm{act}}$ for the actuated case and $c_{d,x,\mathrm{ref}}$ for the nonactuated case, i.e., reference cases:

$$\Delta c_d = \frac{c_{d,x,\mathrm{ref}} - c_{d,x,\mathrm{act}}}{c_{d,x,\mathrm{ref}}} \times 100, \tag{8}$$

$$c_d = c_{d,p} + c_{d,f} = \frac{F_{\mathrm{pressure},x} + F_{\mathrm{friction},x}}{\frac{1}{2}\rho_\infty u_\infty^2 A_{\mathrm{surf}}} \tag{9}$$

are determined by the pressure force $\mathbf{F}_{\mathrm{pressure}} = \frac{1}{T}\int_T \int_{A_{\mathrm{surf}}} -p\mathbf{n}\, dA\, dt$ and the friction force $\mathbf{F}_{\mathrm{friction}} = \frac{1}{T}\int_T \int_{A_{\mathrm{surf}}} \bar{\bar{\boldsymbol{\tau}}}\mathbf{n}\, dA\, dt$ in the streamwise direction, with $F_{\mathrm{pressure},x}$ and $F_{\mathrm{friction},x}$ acting on the wetted surface A_{surf} shown in Fig. 1 by the red-shaded integration window ($155 < x/\theta < 205$). The sampling time for the time average coefficient calculation is denoted by T. Furthermore, the NPS is defined by

$$\Delta P_{\mathrm{net}} = \frac{P_{\mathrm{ref}} - (P_{\mathrm{act}} + P_{\mathrm{control}})}{P_{\mathrm{ref}}} \times 100 = \Delta c_d - \frac{P_{\mathrm{control}}}{P_{\mathrm{ref}}} \times 100, \tag{10}$$

where $P_{\mathrm{ref/act}} = F_{\mathrm{ref},x/\mathrm{act},x} u_\infty$ is the free-stream energy for the reference or actuated case, while $P_{\mathrm{control}} = \frac{1}{T}\int_T \int_{A_{\mathrm{surf}}} [-p\mathbf{u}_{\mathrm{wall}} + \bar{\bar{\boldsymbol{\tau}}}\mathbf{u}_{\mathrm{wall}}] \cdot \mathbf{n}\, dA\, dt$ is the power required to overcome the compressive and frictional forces acting on the plate surface [9,23], where the wall velocity $\mathbf{u}_{\mathrm{wall}} = (0, \quad v_{\mathrm{wall}}, \quad 0)$.

The time averaged sampling error for DR and NPS is considered. The standard uncertainty of DR is calculated by $\sigma_{\mathrm{DR}} = c_{d,x,\mathrm{act}}/c_{d,x,\mathrm{ref}} \sqrt{(\delta c_{d,x,\mathrm{act}}/c_{d,x,\mathrm{act}})^2 + (\delta c_{d,x,\mathrm{ref}}/c_{d,x,\mathrm{ref}})^2}$ [26], where

the standard uncertainty of $\delta c_{d,x,\mathrm{act}}$ and $\delta c_{d,x,\mathrm{ref}}$ is determined by an autoregressive method [27]. Analogous to the calculation of the standard uncertainty of DR, the standard uncertainty of the NPS yields $\sigma_{\mathrm{NPS}} = \sigma_{\mathrm{DR}} + P_{\mathrm{control}}/P_{\mathrm{ref}}\sqrt{(\delta P_{\mathrm{control}}/P_{\mathrm{control}})^2 + (\delta P_{\mathrm{ref}}/P_{\mathrm{ref}})^2}$. Finally, the statistical error is obtained for a confidence interval of 97.5%.

The sampling starts when the quasisteady state is reached, which is determined by the time series of the drag force. For the reference case, data are sampled when $t^+(= tu_\tau^2/\nu) > 2000$, and $\Delta t^+ \approx 5000$ is used to determine the mean value. The maximum sampling error of DR represented by δ_{DR} is less than $\pm 0.20\%$. For the actuation cases, the flow field of the reference case is used as initial distribution and the transition from a nonactuated to an actuated wall flow is performed via a temporal decay function. After an adequate transition interval $\Delta t^+ \approx 4000$, the data of all cases are averaged over $\Delta t^+ \approx 8000$, which equals 50 cycles for the largest period $T^+ = 160$. The sampling errors for the actuation cases will be further discussed in Sec. III A.

III. RESULTS

In this section, the effects of spanwise traveling transversal surface waves (STTSW) on turbulent boundary layers at Mach numbers $M_1 = 0.2$ and $M_2 = 0.7$ are examined. A thorough discussion of the impact of compressibility on drag reduction (DR) and net power saving (NPS) is presented.

First, drag reduction and net power saving are analyzed for different actuation parameters to identify trends at various Mach numbers. Then, the instantaneous flow fields are investigated to show how the wall actuation modifies the wall pressure distribution and near-wall turbulence structures. Subsequently, changes in turbulence statistics and energy spectra are addressed to emphasize turbulence energy redistribution and its impact on the structure of quasistreamwise vortices. Finally, a detailed discussion of the skin friction decomposition yields detailed insights into the contributions of viscous and turbulence dissipation, streamwise kinetic energy, and heterogeneity in the spanwise and streamwise directions.

A. Drag reduction and net power saving

Figures 2(a) and 2(b) show the maps of DR as a function of λ^+ and T^+ at $M_1 = 0.2$ and $M_2 = 0.7$. At each Mach number, the solution of 36 cases is indicated by grey dots. Cubic interpolation of these data onto an irregular grid over the parameter space $\lambda^+ = 1000, 1500, 2000, 2500, 3000$ and $70 \leqslant T^+ \leqslant 160$ was performed to generate the maps. In Fig. 2(a), the maximum DR for $M_1 = 0.2$ is 19.2% at $(\lambda^+, T^+) = (3000, 88)$. This is consistent with the previous result for $M = 0.1$ [9], which showed 16% drag reduction at a similar actuation condition $(\lambda^+, T^+) = (3000, 90)$. In Fig. 2(b), the drag reduction map for $M_2 = 0.7$ shows a similar distribution. The highest drag reduction values occur in the upper left region of the parameter space. The maximum DR increases to 31.35% at the actuation parameter setting $(\lambda^+, T^+) = (3000, 100)$ followed by 27.5% at $(\lambda^+, T^+) = (3000, 88)$. In Fig. 2(c), the differences between $M_1 = 0.2$ and $M_2 = 0.7$ are illustrated. In general, the distribution of the difference of the DR values is positive, indicating that the higher Mach number yields higher DR values. The highest difference is observed in the region in the upper left corner. The entire dataset can be decomposed into two regions, I and II. This decomposition is determined by the critical outer scale parameter, i.e., the phase speed $c = \lambda/T$.The effect of c/u_∞ on DR and NPS is shown in Fig. 3. Figures 3(a) and 3(b) evidence that for increasing c/u_∞ the overall DR tends to increase for each λ^+. This increasing distribution is similar for both Mach numbers. The same is true for the NPS distribution in Figs. 3(c) and 3(d). Considering the DR and NPS distributions, it is clear that at a certain value of c/u_∞ an almost discontinuous increase in DR and a decrease in NPS occur. This division is defined by the red dashed vertical line which also decomposes the difference map in Fig. 2(c) into regions I and II.

Unlike the distribution of DR as a function of c/u_∞ in Fig. 3(a), which strongly oscillates, Fig. 4(a) indicates a linear correlation between DR and the scaling parameter $Ac/\theta u_\infty$ for each λ^+ at $M_1 = 0.2$. The nondimensional parameter $Ac/\theta u_\infty$ captures the combined effect of wave amplitude

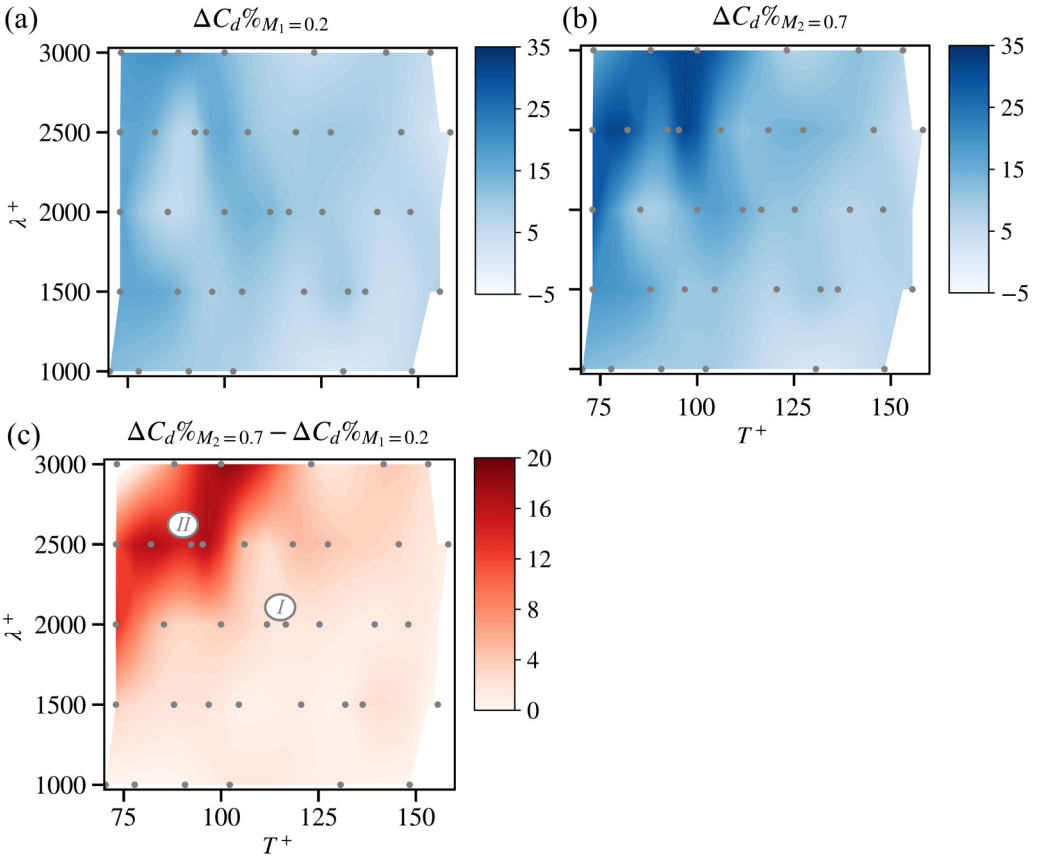


FIG. 2. Maps of DR at (a) $M_1 = 0.2$ and (b) $M_2 = 0.7$. Map of the difference in DR between $M_1 = 0.2$ and $M_2 = 0.7$ (c).

A and speed c which describe the degree of influence the actuation has on modifying near-wall turbulence. The linear correlation indicates that quantities A and c are independently positive factors that influence drag reduction at $M_1 = 0.2$. However, at $M_2 = 0.7$ shown in Fig. 4(b), this linear relationship is perturbed by certain outliers. These outliers represent flow solutions in region II in Figs. 2(c) and 3(b), where the phase velocity c becomes the dominant factor for drag reduction. Therefore, we hypothesize that the drag reduction mechanism may differ between regions I and II illustrated in Figs. 2 and 3.

To investigate potential differences, the subsequent analysis focuses on representative cases selected from each region. Specifically, the cases achieving the maximum drag reduction at $M = 0.2$ in each region are chosen. For comparative purposes, the same actuation parameters are applied at $M = 0.7$. In Table II, the essential parameters and findings of four characteristic cases from regions I and II at $M_1 = 0.2$ and $M_2 = 0.7$ are summarized. The cases from region I (CI) with $c/u_\infty = 0.95$ show a slight increase in Δc_d and a poor increase in ΔP_{net} at increasing Mach number. This trend agrees with the results from Ruby and Foysi [15], who observed that drag reduction and net power saving tend to improve with increasing Mach number. However, in region II (CII) with a nondimensional phase speed $c/u_\infty = 1.54$, there is a large increase in Δc_d, while ΔP_{net} shows an order of magnitude reduction at $M_2 = 0.7$ caused by the drastic increase in P_{control}. The net power saving is defined in Eq. (10) by the difference between Δc_d and the power for control. That is, positive values are achieved only when Δc_d, i.e., drag reduction, surpasses the control power. The

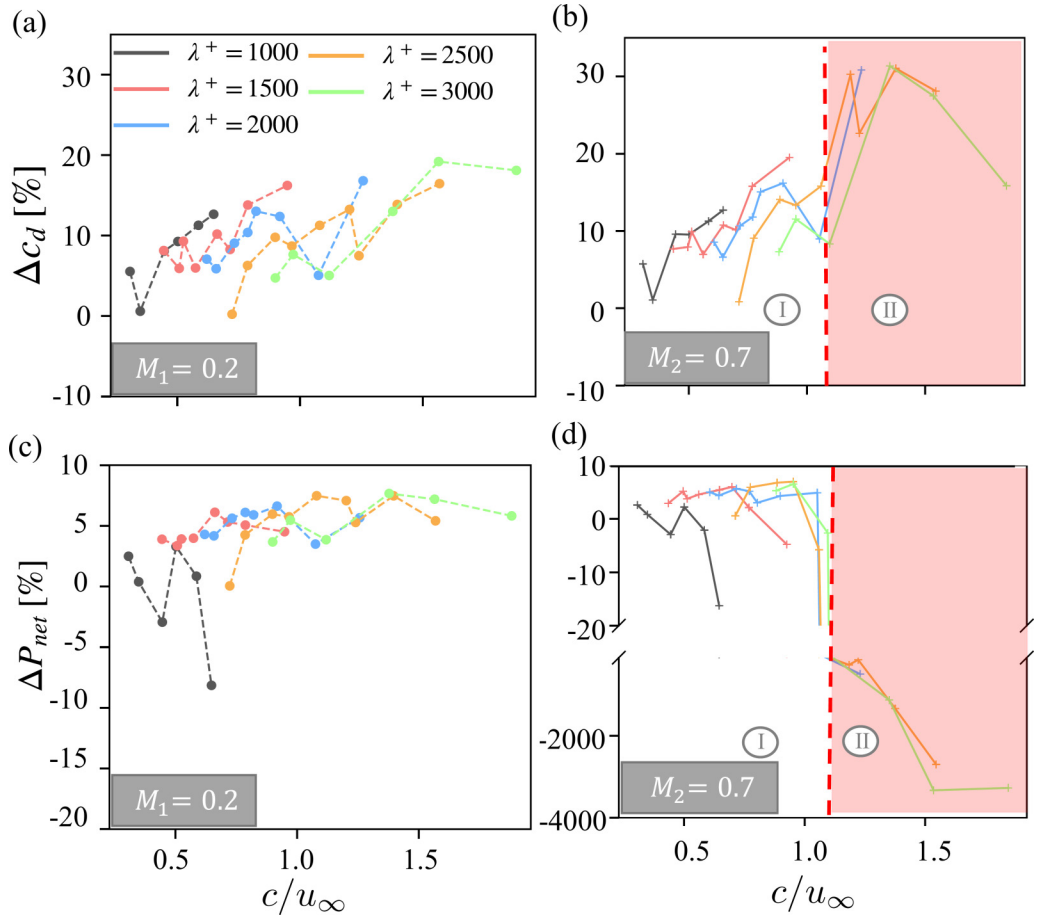


FIG. 3. DR (a), (b) and NPS (c), (d) as a function of phase speed c/u_∞ at (a), (c) $M_1 = 0.2$ and (b), (d) $M_2 = 0.7$.

statistical error for drag reduction δ_{DR} is less than $\pm 0.25\%$; for δ_{NPS}, in region I it is less than $\pm 0.34\%$ and in region II it is less than $\pm 0.55\%$ at $M_1 = 0.2$ and $\pm 4.4\%$ at $M_2 = 0.7$. In actuated flat plate flow, drag reduction is influenced primarily by the friction force, while the pressure-related force $\frac{1}{T}\int_T \int_{A_{\mathrm{surf}}} [-p\mathbf{u}_{\mathrm{wall}}] \cdot \mathbf{n}\, dA\, dt$ is essential for the control power. A more detailed analysis of the impact of the pressure and shear stress distribution is given in the next section.

B. Instantaneous flow field

Figire 5 shows for several turbulent boundary layer flows wall pressure $p_{\mathrm{wall}}/p_\infty$, pressure contours in the yz plane, and λ_2 contours [28] in the xz plane at $y^+ < 60$. The λ_2 contours are illustrated for $\lambda_2^+ = -0.03$ and colored by the relative Mach number $M_{\mathrm{rel}} = \sqrt{u^2 + v^2 + (w-c)^2}/\sqrt{\gamma p/\rho}$. They represent streamwise coherent structures that are massively determined by the shear stress in the streamwise direction. The flow fields possess spanwise inhomogeneities with periodic pressure and shear stress patterns. The trough region is characterized by higher pressure, while the crest region features greater near-wall velocity, i.e., higher total shear.

The wall deformation generates a compression region in approximately $0 < z^+ < 1500$ and an expansion region in approximately $1500 < z^+ < 3000$. This is especially evident in Fig. 5(f). A spanwise shock wave develops at $M_2 = 0.7$. In the leeward region of the surface wave

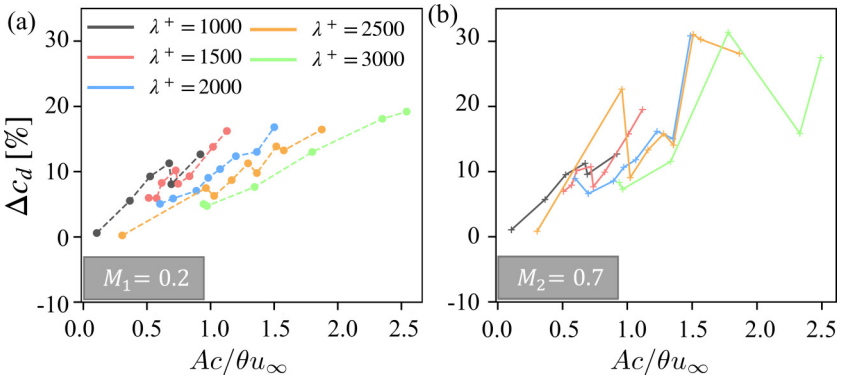


FIG. 4. DR as a function of $Ac/\theta u_\infty$ at (a) $M_1 = 0.2$ and (b) $M_2 = 0.7$.

$1500 < z^+ < 3000$, the flow undergoes a massive acceleration. At the high phase speed $c/u_\infty = 1.54$, the flow is supersonic such that the compression in the windward region of the surface wave causes the formation of a shock wave. This is evidenced by the wall pressure distribution and pressure contours shown in Fig. 5(f). Upstream of the shock wave, the streamwise vortices are less dense in the near-wall region, while just downstream of the shock the high pressure causes a locally extremely high concentration of the streamwise vortices. That is, the high speed c/u_∞ causes at $M_2 = 0.7$ a high wall-shear stress just downstream of the shock while most of the surface of the wave experiences a low wall-shear stress distribution.

Figure 6 shows distributions of the time-phase averaged skin-friction coefficient, pressure coefficient, and power induced by the pressure force $\frac{1}{T}\int_T \int_{A_{\text{surf}}} [-pv_{\text{wall}}]\, dA\, dt$ at $x/\theta = 180$. The averages are obtained by first aligning the phase to the initial state such that they represent an exact cosine shape without any phase shift. Then, the spanwise average along the fixed streamwise position $x^+ = 2000$, which is shown by the horizontal line in Fig. 5, is determined. The phase averaged skin-friction coefficient $\langle c_f \rangle_{\text{def}}$ is defined as the ratio of the phase-averaged wall-shear stress to the dynamic pressure:

$$\langle c_f \rangle_{\text{def}} = \mu \frac{\partial \langle u \rangle}{\partial y} \Big/ \frac{1}{2} \rho_\infty u_\infty^2. \tag{11}$$

It shows a phase shift between the two Mach numbers in regions I and II. That is, the variation of the Mach number causes the phase shift. The influence of the actuation in the y direction gradually propagates to the x direction, which modifies the u velocity component. The $\langle c_f \rangle_{\text{def}}$ for $M_2 = 0.7$ in region II agrees with the streamwise vortices distribution in Fig. 5(f). Upstream of the shock wave the sparse distribution of the near-wall streamwise vortices corresponds to a

TABLE II. Actuation parameters of selected cases from regions I and II for $M_1 = 0.2$ and $M_2 = 0.7$. The actuation parameters in inner scaling include wave amplitude A^+, period T^+, and wavelength λ^+. The phase speed c is nondimensionalized by the freestream velocity u_∞. Besides the time average data of Δc_d, $P_{\text{control}}/P_{\text{ref}}$, and ΔP_{net}, the statistical errors δ_{DR} and δ_{NPS} for a 97.5% confidence interval are listed.

Case	M	Region	A^+	T^+	λ^+	c/u_∞	Δc_d	δ_{DR}	$\frac{P_{\text{control}}}{P_{\text{ref}}}$	ΔP_{net}	δ_{NPS}
CIM02	0.2	I	63	141	3000	0.95	7.65	±0.25	2.18	5.47	±0.34
CIIM02	0.2	II	74	88	3000	1.54	19.20	±0.24	12.00	7.20	±0.55
CIM07	0.7	I	63	141	3000	0.95	11.78	±0.25	4.96	6.82	±0.32
CIIM07	0.7	II	74	88	3000	1.54	27.57	±0.21	3357.37	−3329.80	±4.4

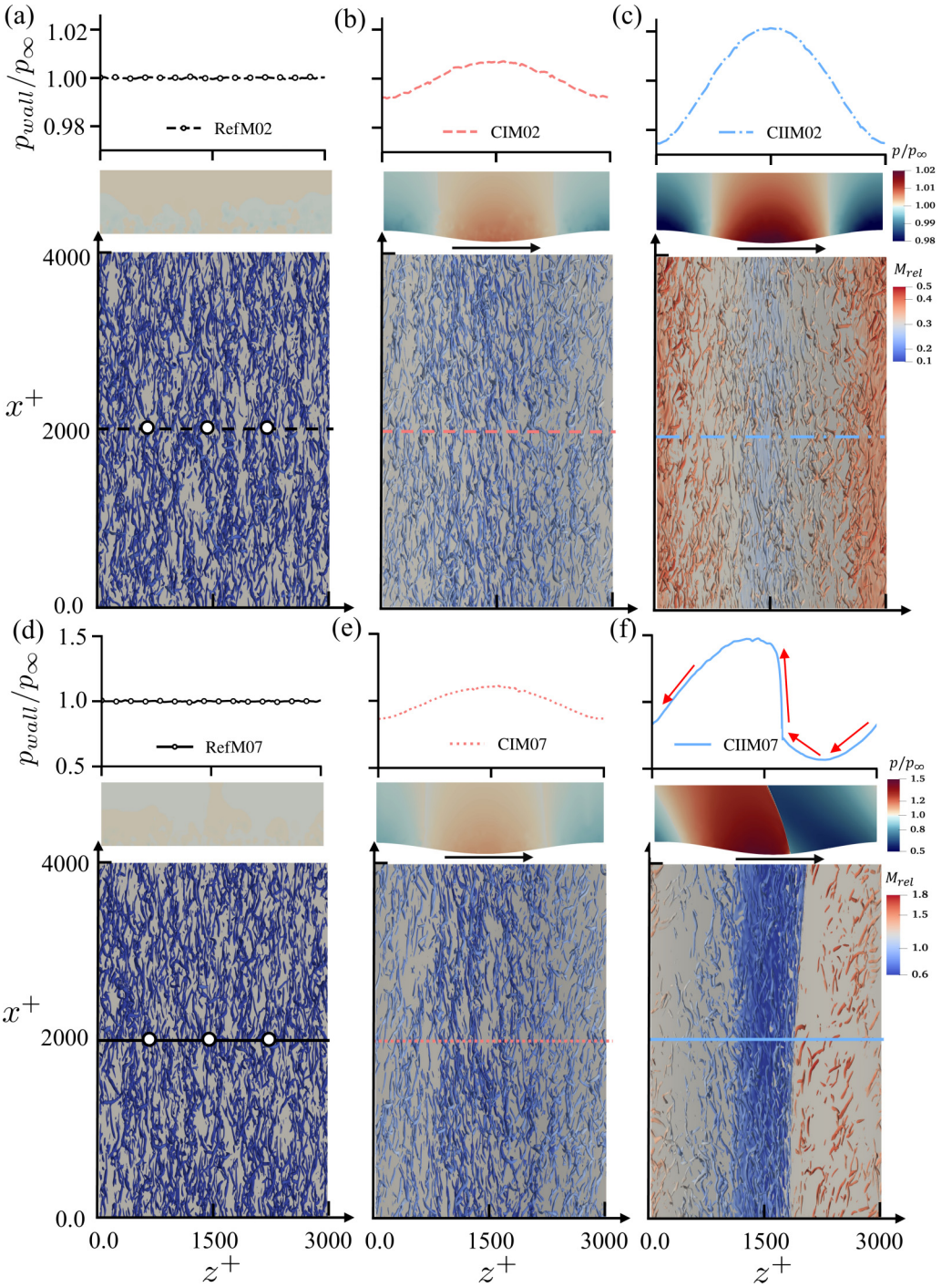


FIG. 5. Instantaneous flow field for (a), (d) nonactuated reference cases, actuated cases of (b), (e) CI and (c), (f) CII, at (a)–(c) $M_1 = 0.2$ and (d)–(f) $M_2 = 0.7$. Each illustration consists of wall pressure distribution, pressure contours in the yz plane at $x/\theta = 180$, and λ_2 contours in the xz plane at $y^+ < 60$. The black arrows below the pressure contours illustrate the propagation direction of the surface wave. The red arrows in panel (f) represent the direction and relative magnitude of the pressure gradients caused by the wall deformation.

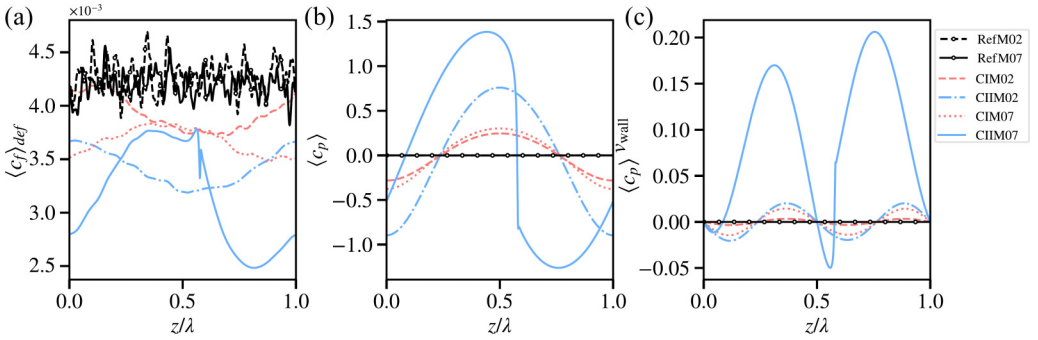


FIG. 6. Time and phase averaged (a) streamwise skin-friction coefficient $\langle c_f \rangle_{\text{def}}$, (b) pressure coefficient $\langle c_p \rangle$, and (c) the product of pressure coefficient and wall velocity $\langle c_p \rangle v_{\text{wall}}$ at $x/\theta = 180$.

lower $\langle c_f \rangle_{\text{def}}$, and downstream of the shock wave the compression of the flow due to the shock amplifies the wall-bounded turbulent structures, resulting in larger $\langle c_f \rangle_{\text{def}}$. This corresponds to the relationship between streamwise vortices and wall-shear stress [29]. However, as shown in Fig. 6(b), the formation of shock waves disrupts the sinusoidal pattern of $\langle c_p \rangle$. Furthermore, the product $\langle c_p \rangle v_{\text{wall}}$ which is directly proportional to the control power is influenced by this disruption. The asymmetry in $\langle c_p \rangle$ leads to an increase in P_{control}, which is evidenced by the large net integral area in Fig. 6(c). This means that the formation of the shock waves requires extra energy input. In other words, shock waves do lower net power saving. To further investigate the impact of the formation of shock waves on the flow, turbulent statistics, turbulence scales, and production and dissipation of turbulent kinetic energy for flow cases without and with shock waves will be analyzed.

C. Flow statistics

Figure 7 presents the spanwise averaged, wall-normal distribution of the mean streamwise velocity, $\overline{u/u_\tau}$. The reduced wall velocity gradient for the actuated cases in Fig. 7(b) suggests a decrease in wall-shear stress, i.e., lower skin friction. The upward shift in the velocity profile in Fig. 7(c) is known from various wall-bounded turbulent flows where effective drag reduction techniques have been applied in simulations [26] and experiments [30]. The upward shift in the velocity profile is a rebalancing between turbulence energy production and viscous dissipation which yields a thickened viscous sublayer and a shortened logarithmic layer. This adjustment leads to a decrease in turbulence energy production and reduced turbulent drag [31]. Gatti and Quadrio [26] thoroughly investigated this vertical shift and showed that it provides a robust measure of drag reduction. Their work confirms that the magnitude of the vertical shift directly correlates with drag reduction. Similarly, the size of the shift in Fig. 7(c) is primarily determined by the level of drag reduction, independent of the Mach number. In Fig. 7(d), the diagnostic function $y^* \frac{d\overline{u}^*}{dy^*}$, which is used to identify the logarithmic region more precisely, is presented. The logarithmic region, which is characterized by the inverse of the von Kármán constant ($\kappa^{-1} \approx 2.63$), is evident in Fig. 7(d). For the nonactuated reference case at $\text{Re}_\tau \approx 360$, this region ranges $40 \lesssim y^* \lesssim 100$, whereas in the study by Lozano-Durán and Jiménez [32] it spans $40 \lesssim y^* \lesssim 140$ at $\text{Re}_\tau = 550$. For the actuated cases, a clear shortening of the logarithmic region is observed. When drag reduction increases, the size of the logarithmic region is reduced.

The distributions of the Reynolds stress components $\widehat{u'''u'''}$, $\widehat{v'''v'''}$, $\widehat{w'''w'''}$, and the premultiplied production of turbulent kinetic energy yP are illustrated in Fig. 8. The results allow a quantitative analysis of the net modifications in near-wall turbulence induced by the moving wall using two inner scalings $u_{\tau,\text{ref}}$ and $u_{\tau,\text{act}}$. The clear reductions in turbulence intensities and energy production shown in Figs. 8(a), 8(c), 8(e), and 8(g) highlight the impact of the moving wall.

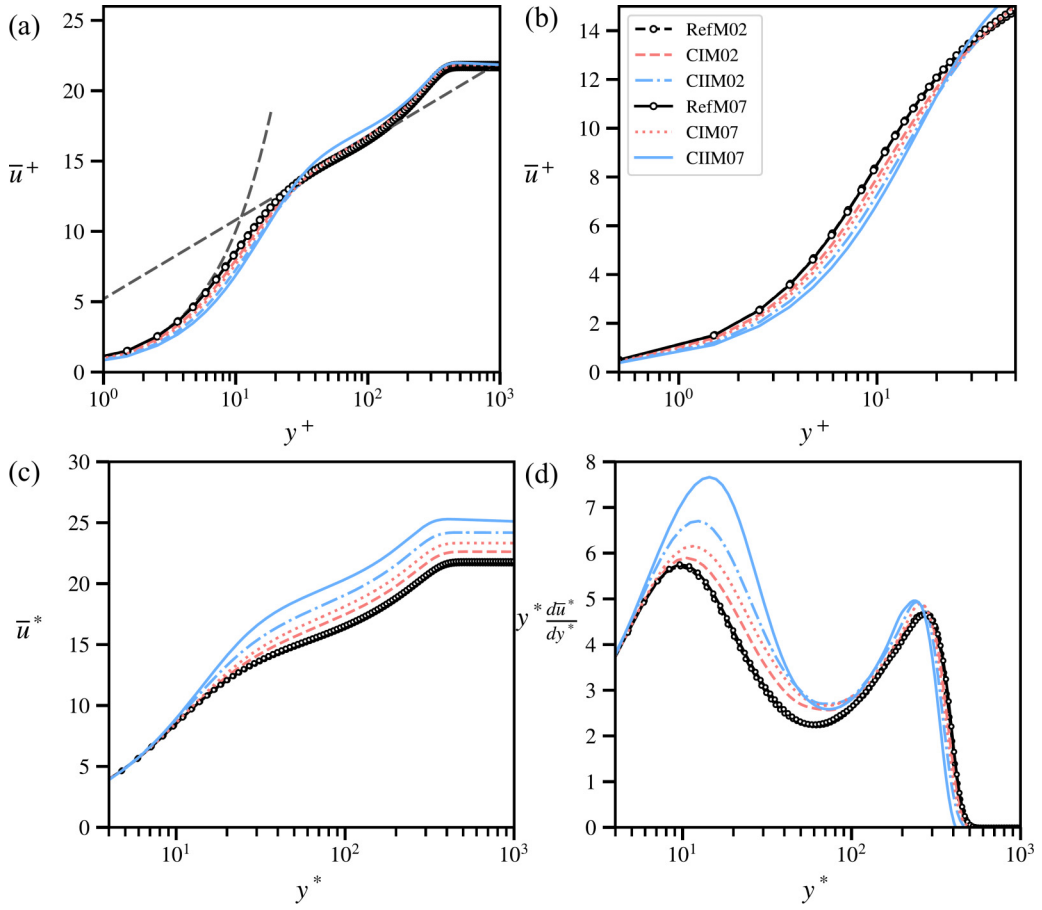


FIG. 7. Spanwise averaged wall-normal distribution of the mean streamwise velocity at $x/\theta = 180$, (a) scaled by the friction velocity of the nonactuated case $u_{\tau,\mathrm{ref}}$, denoted by the superscript $+$; (b) an enlargement of the near-wall region of (a); (c) scaled by the friction velocity of the actuated case $u_{\tau,\mathrm{act}}$, denoted by the superscript $*$; (d) diagnostic function $y^* \frac{d\overline{u}^*}{dy^*}$ for the profile in (c).

The spanwise averaged Reynolds stress component of the wall-normal velocity $\widehat{\overline{v'''v'''}}^*$ in Fig 8(d) shows a good overlap with the reference cases. This indicates that the symmetric wavy wall actuation does not significantly alter the turbulence intensity in the wall-normal direction. However, when shock waves occur, significant changes are observed up to the logarithmic layer with an obvious attenuation of $\widehat{\overline{v'''v'''}}^*$. Likewise, the spanwise velocity component $\widehat{\overline{w'''w'''}}^*$ in Fig. 8(f) loses similarity between the actuated and nonactuated cases due to the induced net mass flow in the spanwise direction [9]. From Fig. 8(b), it is evident that the peak of the streamwise velocity fluctuations below the buffer layer is significantly reduced. The spanwise forcing leads to a reorganization of the near-wall turbulent structures such that the turbulent kinetic energy is redistributed from the streamwise to the spanwise component. The dominance of the streamwise fluctuations is mitigated. These findings agree with the results of Gattere *et al.* [24], who showed that similar spanwise actuation strategies significantly modify turbulence dynamics and contribute to the reduction of streamwise fluctuation intensity. A shift in the peak production of turbulent kinetic energy that mirrors the behavior seen in Fig. 8(b) is shown in Fig. 8(h). The peak is clearly displaced in the inner layer. This is especially true for the cases with shock waves. This result indicates that

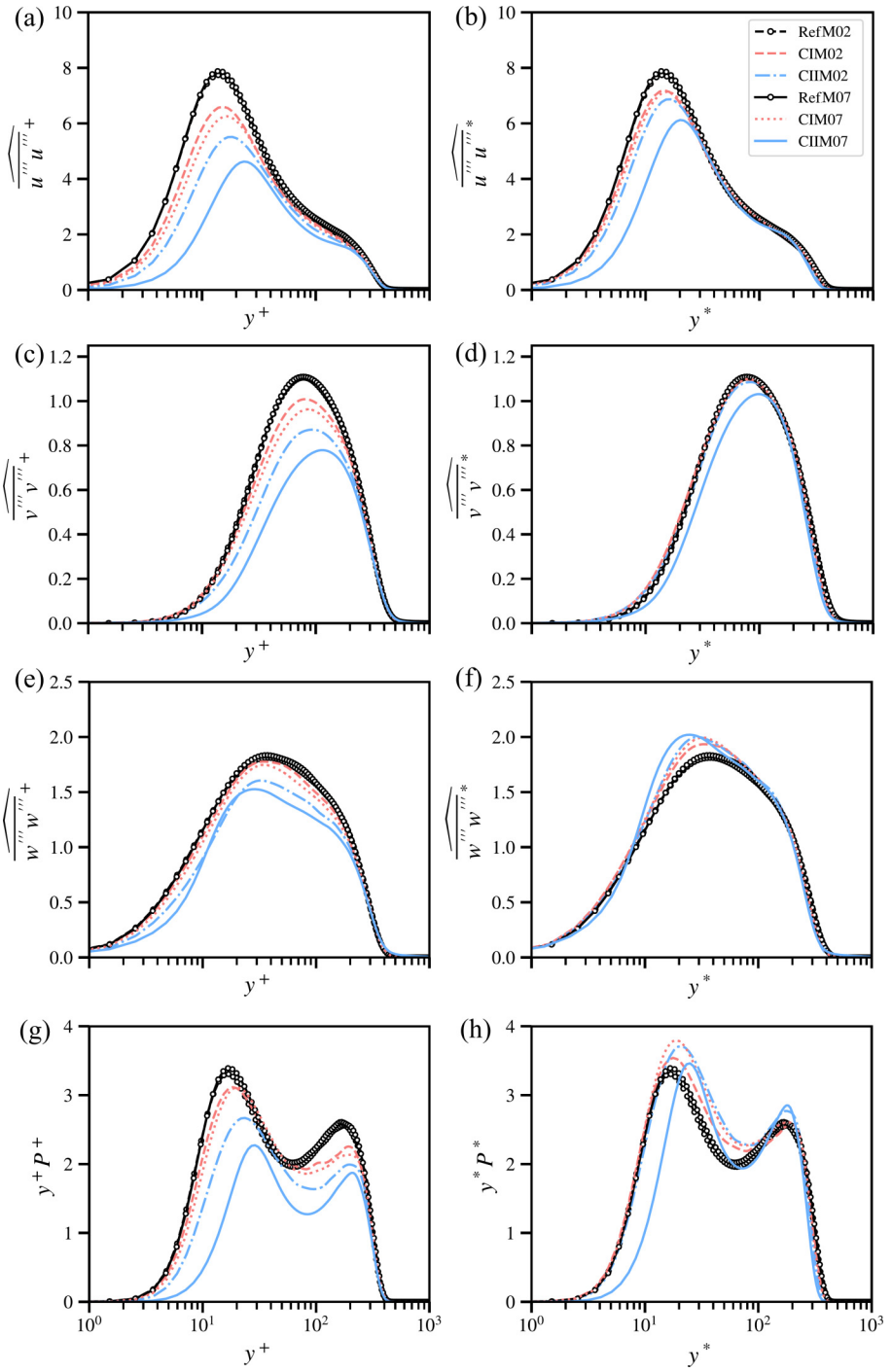


FIG. 8. Spanwise averaged wall-normal distributions of Reynolds stress components and turbulence production at $x/\theta = 180$, scaled by (a), (c), (e), (g) the friction velocity of the nonactuated case $u_{\tau,\mathrm{ref}}$; (b), (d), (f), (h) scaled by the friction velocity of the actuated case $u_{\tau,\mathrm{act}}$. Reynolds stress profiles for (a), (b) streamwise velocity, (c), (d) wall-normal velocity, (e), (f) spanwise velocity, and (g), (h) premultiplied production of turbulent kinetic energy.

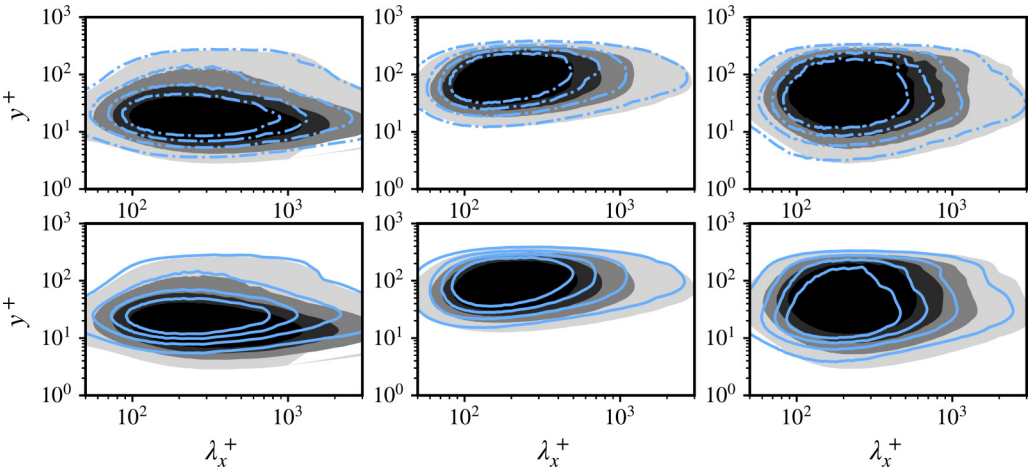


FIG. 9. Streamwise premultiplied spectra $k_x\phi_{u_i'''u_i'''}$ of (left column) the streamwise, (center column) the wall-normal, and (right column) the spanwise stochastic velocity fluctuations for case II at $M_1 = 0.2$ (CIIM02) (top) and $M_2 = 0.7$ (CIIM07) (bottom). The blue lines represent the actuated case, while the white-to-black contours indicate the reference case. The contour and line levels correspond to 0.15, 0.3, 0.45, and 0.6 of the maximum spectra for each case.

the near-wall part of the boundary layer is significantly modified. The spanwise actuation reduces the streamwise fluctuations and alters the location and intensity of the turbulent kinetic energy production.

Figure 9 presents the streamwise premultiplied one-dimensional (1D) spectra of the stochastic velocity fluctuations $k_x\phi_{u_i'''u_i'''}$ for case II at $M_1 = 0.2$ (top) and $M_2 = 0.7$ (bottom). The quantity k_x is the streamwise wavenumber and $\phi_{u_i'''u_i'''}$ is the Fourier coefficient of $u_i'''u_i'''$. Due to the minor differences for case I between $M_1 = 0.2$ and $M_2 = 0.7$ those spectral results are not shown here. The streamwise extent, where 60% of the maximum spectra of $u'''u'''$ occur, is reduced from the range $95 \lesssim \lambda_x^+ \lesssim 1001$ in the nonactuated case to $76 \lesssim \lambda_x^+ \lesssim 896$ for case II at $M_1 = 0.2$. Similarly, the range is reduced from $94 \lesssim \lambda_x^+ \lesssim 1020$ to $79 \lesssim \lambda_x^+ \lesssim 854$ at $M_2 = 0.7$. A comparable decrease of the scale structures is observed in the spectra of $v'''v'''$ and $w'''w'''$. Additionally, the contours rotate counterclockwise relative to the non-actuated cases. The spectral peak shifts to larger y^+ values, e.g., from $y^+ \approx 15$ to $y^+ \approx 18$ at $M_1 = 0.2$ and from $y^+ \approx 15$ to $y^+ \approx 23$ at $M_2 = 0.7$ in the $u'''u'''$ spectra.

The spanwise premultiplied 1D spectra of the diagonal component of the Reynolds stress tensor $k_z\phi_{u_i'''u_i'''}$ are shown in Fig. 10, where k_z is the spanwise wave number. The spanwise energy spectra of the diagonal components reach a peak at $\lambda_z^+ \approx 100$ for the nonactuated cases, which agrees with the near-wall coherent structures identified in [33]. The energetic peak in $k_z\phi_{u'''u'''}$ for the actuated case occurs at higher y^+ and λ_z^+ values for $M_2 = 0.7$, while there is only a minor shift for $M_1 = 0.2$. The energy distribution shifts to larger spanwise scales (λ_z^+), which indicates an elongation in the spanwise direction. Simultaneously, a compression of the quasistreamwise vortices (QSV) in the streamwise direction is observed in Fig. 9 by a shift to smaller streamwise wavelengths (λ_x^+). That is, due to the impact of the shock waves on the near-wall flow the quasistreamwise vortices become shorter in the streamwise direction and are extended in the spanwise direction. This indicates a more isotropic turbulent energy distribution for the smaller-scale structures, while still maintaining streamwise directional characteristics. Furthermore, the energy center shifts off the wall into regions of lower shear. The spectra patterns of $v'''v'''$ and $w'''w'''$ show more diffuse energy distributions that spread over a wider range of spanwise scales. The spanwise traveling shock wave interacts with the quasistreamwise vortices and decomposes the large vortices into smaller substructures. The contours

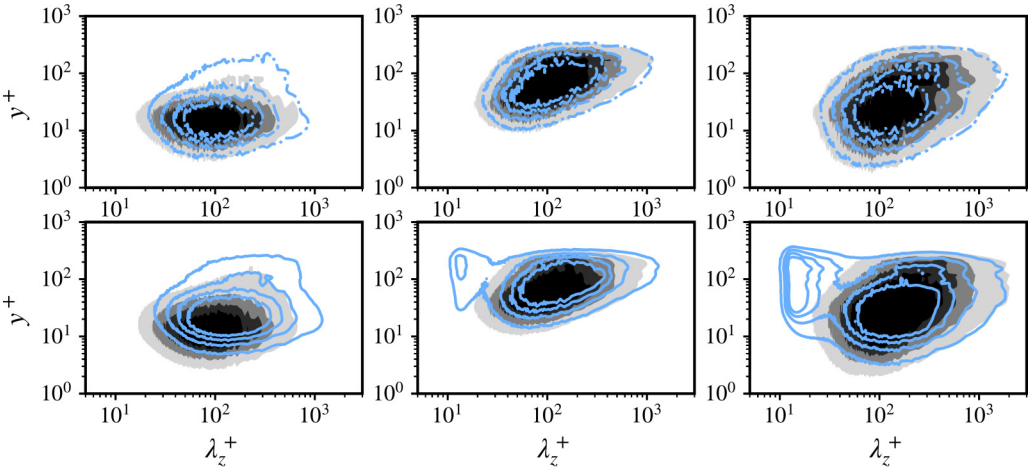


FIG. 10. Spanwise premultiplied spectra $k_z\phi_{u_i''u_i''}$ of (left column) the streamwise, (center column) the wall-normal, and (right column) the spanwise stochastic velocity fluctuations for case II at $M_1 = 0.2$ (CIIM02) (top) and $M_2 = 0.7$ (CIIM07) (bottom). The blue lines represent the actuated case, while the white-to-black contours indicate the reference case. The contour and line levels correspond to 0.15, 0.3, 0.45, and 0.6 of the maximum spectra for each case.

indicate distinctive patterns at lower λ_z^+ illustrating this decomposition. The energy is concentrated at smaller spanwise scales (λ_z^+) resulting in a more diffuse near-wall flow structure.

D. Skin friction decomposition

The skin-friction decomposition is based on integrating the mean flow quantities in the wall-normal direction such that quantities on the wall are obtained [34]. Two decomposition methods are widely used: the Fukagata-Iwamoto-Kasagi (FIK) [35] identity and the Renard-Deck (RD) [36] identity. The FIK identity, which is based on a threefold integration of the streamwise momentum conservation equation, was further developed in recent studies [37,38] and is often used in turbulent flow and drag reduction analyses [14]. However, the repeated integration in the FIK identity can result in terms that lack clear physical interpretation [36,39,40]. Moreover, Ricco and Skote [41] showed an additional limit of the FIK decomposition in boundary layer flows. The required vertical truncation renders the individual terms dependent on the integration bound, which undermines their physical interpretability. If the upper bound reaches infinity, the decomposition degenerates into the von Kármán integral relation and offers little diagnostic insight.

The RD identity provides a more physically informed decomposition by integrating the conservation law of mean kinetic energy in the flow reference frame for incompressible flow. This method was extended by Li *et al.* [42] to compressible zero pressure gradient turbulent boundary layers. Further modifications are made to adapt the RD identity to the current 3D STTSW actuated flow field by addressing the inhomogeneity in the spanwise direction and incorporating phase-Favre averaging.

Using the notation from Sec. II C and the continuity equation and phase-Favre averaging for the three-dimensional Reynolds-averaged momentum equation in the streamwise direction,

$$\frac{\partial\langle\rho uu\rangle}{\partial x}+\frac{\partial\langle\rho uv\rangle}{\partial y}+\frac{\partial\langle\rho uw\rangle}{\partial z}=-\frac{\partial\langle p\rangle}{\partial x}+\frac{1}{\mathrm{Re}_0}\left(\frac{\partial\langle\tau_{xx}\rangle}{\partial x}+\frac{\partial\langle\tau_{yx}\rangle}{\partial y}+\frac{\partial\langle\tau_{wx}\rangle}{\partial z}\right), \tag{12}$$

yields

$$\langle\rho\rangle\frac{D\hat{u}}{Dt}+\langle\rho\rangle\left(\frac{\partial\widehat{u'''u'''}}{\partial x}+\frac{\partial\widehat{u'''v'''}}{\partial y}+\frac{\partial\widehat{u'''w'''}}{\partial z}\right)=-\frac{\partial\langle p\rangle}{\partial x}+\frac{1}{\mathrm{Re}_0}\left(\frac{\partial\langle\tau_{xx}\rangle}{\partial x}+\frac{\partial\langle\tau_{yx}\rangle}{\partial y}+\frac{\partial\langle\tau_{wx}\rangle}{\partial z}\right), \tag{13}$$

with

$$\frac{D\hat{u}}{Dt}=\hat{u}\frac{\partial\hat{u}}{\partial x}+\hat{v}\frac{\partial\hat{u}}{\partial y}+\hat{w}\frac{\partial\hat{u}}{\partial z}.$$

Following the approach of the Renard-Deck (RD) identity [36], we construct the kinetic energy equation by multiplying Eq. (13) by $\hat{u}$. Subsequently, the initial wall reference frame is transformed to a fluid reference frame where the wall moves with velocity $-u_\infty$. Finally, after integrating from the wall to infinity and transforming back to the original reference frame, the phase averaged skin-friction coefficient is decomposed:

$$\begin{aligned}\langle c_f\rangle=&\underbrace{\frac{2}{\rho_\infty u_\infty^3\mathrm{Re}_0}\int_0^\infty\langle\tau_{yx}\rangle\frac{\partial\hat{u}}{\partial y}\,\mathrm{d}y}_{c_{f1}}+\underbrace{\frac{2}{\rho_\infty u_\infty^3}\int_0^\infty\langle\rho\rangle(\widehat{-u'''v'''})\frac{\partial\hat{u}}{\partial y}\,\mathrm{d}y}_{c_{f2}}\\&+\underbrace{\frac{2}{\rho_\infty u_\infty^3}\int_0^\infty\langle\rho\rangle(\hat{u}-u_\infty)\left(\hat{u}\frac{\partial\hat{u}}{\partial x}+\hat{v}\frac{\partial\hat{u}}{\partial y}+\hat{w}\frac{\partial\hat{u}}{\partial z}\right)\mathrm{d}y}_{c_{f3}}\\&+\underbrace{\frac{2}{\rho_\infty u_\infty^3}\int_0^\infty(\hat{u}-u_\infty)\frac{\partial}{\partial x}\left(\langle\rho\rangle\widehat{u'''u'''}-\frac{\langle\tau_{xx}\rangle}{\mathrm{Re}_0}+\langle p\rangle\right)\mathrm{d}y}_{c_{f4}}\\&+\underbrace{\frac{2}{\rho_\infty u_\infty^3}\int_0^\infty(\hat{u}-u_\infty)\frac{\partial}{\partial z}\left(\langle\rho\rangle\widehat{u'''w'''}-\frac{\langle\tau_{wx}\rangle}{\mathrm{Re}_0}\right)\mathrm{d}y}_{c_{f5}}.\end{aligned} \tag{14}$$

The quantity c_{f1} represents the viscous dissipation, c_{f2} corresponds to turbulent dissipation, c_{f3} denotes the variation of kinetic energy in the streamwise direction, c_{f4} describes streamwise heterogeneity, and c_{f5} accounts for spanwise heterogeneity. Note that the sum $c_{f3}+c_{f4}$ represents the flow development in the streamwise direction.

The Renard-Deck decomposition (RD) identity was effectively used in the analysis of turbulent flows and in flow control strategies involving blowing and suction [44,45] or spanwise in-plane wall oscillations [15]. The validation of the RD identity is presented in Fig. 11. For the nonactuated case, the computed skin-friction coefficient shows excellent agreement with the empirical formula $\langle c_f\rangle_{\mathrm{emp}}=0.024\times\mathrm{Re}_\theta^{-0.25}$ [43]. There is a close agreement between $\langle c_f\rangle_{\mathrm{def}}$ and the sum of all contribution terms in Eq. (14) for $M_1=0.2$ or $M_2=0.7$. It is important to note that the relative errors determined by $(\overline{c_{f1}}+\overline{c_{f2}}+\overline{c_{f3}}+\overline{c_{f4}}+\overline{c_{f5}}-\overline{c_f}_{\mathrm{def}})/\overline{c_f}_{\mathrm{def}}$ are well within $\pm1.3\%$ and as such validate the reliability of this decomposition. To further explore the local impact of spanwise periodic actuation on skin friction, the contributions of each term in the decomposition at specific spatial locations are analyzed in detail in the following.

Figue 12 provides a comprehensive view of the spanwise distribution of the components of the RD identity at $x/\theta=180$. Each diagram shows how different elements of the skin-friction decomposition vary across the spanwise direction z/λ for the nonactuated and actuated cases at two Mach numbers. For the viscous dissipation component $\langle c_{f1}\rangle$, a distinct sinusoidal pattern in the actuated cases that follows the behavior of c_f illustrated in Fig. 6(a) is evident in Fig. 12(a). This agreement between the total c_f and $\langle c_{f1}\rangle$ suggests that viscous dissipation is a major contributor to overall skin

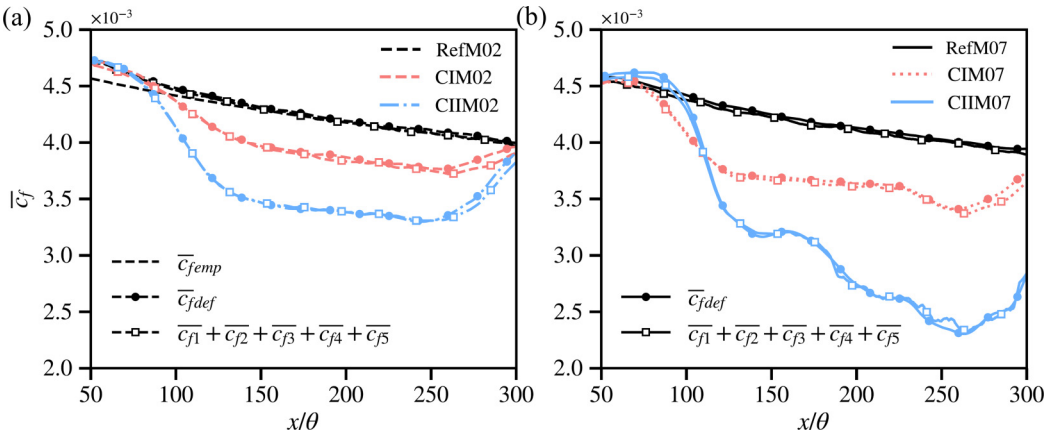


FIG. 11. The spanwise-averaged skin-friction coefficient distribution in the streamwise direction for cases at (a) $M_1 = 0.2$ and (b) $M_2 = 0.7$. The black dashed line in (a) indicates the empirical correlation $\langle c_f \rangle_{\text{emp}} = 0.024 \times \text{Re}_\theta^{-0.25}$ [43] which was developed for incompressible flows. The full circles represent the definition value in Eq. (11). The open square represents the sum of the terms of the RD identity.

friction. In Fig. 12(b), the local fluctuations in $\langle c_{f2} \rangle$ for the nonactuated cases significantly diminish under actuation, which indicates a similar reduction in molecular viscous dissipation. However, unlike $\langle c_{f1} \rangle$, the turbulent component $\langle c_{f2} \rangle$ does not follow a sinusoidal pattern, which is due to the inherent randomness of turbulence. Moreover, the result for $M_2 = 0.7$ generally shows lower $\langle c_{f2} \rangle$ values in the crest regions and higher values in the trough regions compared to $M_1 = 0.2$ when the findings for Mach numbers within the same set of cases are compared. This result substantiates the impact of compressibility on the spanwise distribution of turbulent dissipation. The higher Mach number leads to more pronounced variations in $\langle c_{f2} \rangle$. Finally, in the upstream region $\langle c_{f2} \rangle$ remains small indicating weak turbulent dissipation. At the shock location, a sharp increase in $\langle c_{f2} \rangle$ is observed due to the strong velocity and pressure gradients induced by the shock, which amplifies turbulence production and dissipation. Therefore, the elevated $\langle c_{f2} \rangle$ values indicate enhanced turbulent activity and intensified momentum transfer near the wall downstream of the shock.

Figures 12(c) and 12(d) present the spanwise distribution of the combined streamwise kinetic energy variation, streamwise heterogeneity components $\langle c_{f3} \rangle + \langle c_{f4} \rangle$, and the spanwise heterogeneity component $\langle c_{f5} \rangle$. The fluctuation amplitude in the combined streamwise kinetic energy variation, streamwise heterogeneity component, and spanwise heterogeneity component is significantly reduced in the actuated cases compared to the nonactuated reference case. This reduction indicates that spanwise actuation effectively stabilizes these components and yields a more uniform skin friction distribution across the spanwise direction. In the CIIM07 case, the contributions to the flow development in the streamwise and spanwise heterogeneity are strongly increased upstream of the shock wave but decreased to a lower level downstream of the shock wave. The sum of Figs. 12(e) and 12(f) equals the total c_f in Fig. 6(a). Hence, it is evident that the reduction in the dissipation components outweighs the increase in heterogeneity and flow growth. Therefore, the overall skin friction is still reduced for the case II at $M_2 = 0.7$.

Figure 13 presents a comparison of the normalized skin-friction components c_{f1}, c_{f2}, c_{f3}, c_{f4}, and c_{f5} expressed by the ratio of the total skin friction to the reference skin friction , for several cases for $M_1 = 0.2$ and $M_2 = 0.7$. Unlike the previous analysis that focused on the fixed streamwise location $x/\theta = 180$, this figure is based on data from the entire fully actuated region and as such shows a less local but more global perspective on the impact of actuation. In the nonactuated reference cases, viscous and turbulent dissipation, i.e., c_{f1} and c_{f2}, are the main contributors to total skin friction.

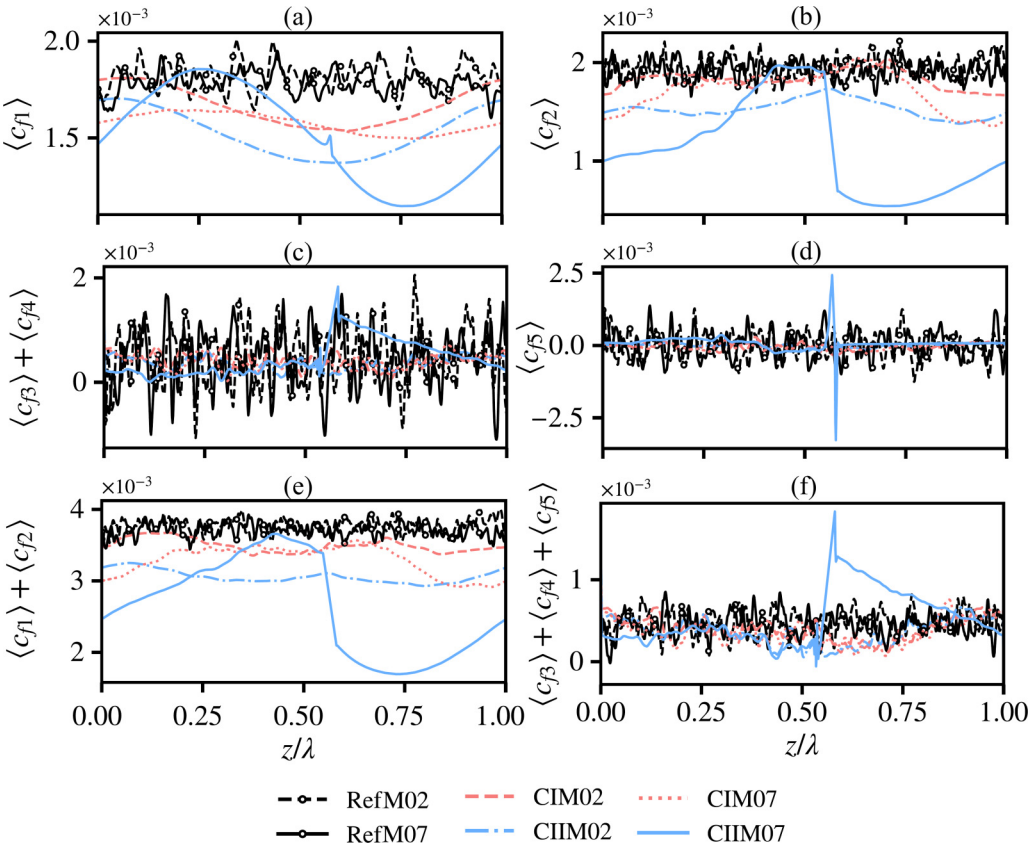


FIG. 12. Distribution of the skin-friction identity in the spanwise direction at $x/\theta = 180$. Variation of (a) viscous dissipation $\langle c_{f1}\rangle$, (b) turbulence dissipation $\langle c_{f2}\rangle$, (c) growth of flow in the streamwise direction $\langle c_{f3}\rangle + \langle c_{f4}\rangle$, (d) spanwise heterogeneity $\langle c_{f5}\rangle$, (e) summation of dissipation $\langle c_{f1}\rangle + \langle c_{f2}\rangle$, and (f) growth of flow in the streamwise and the spanwise directions $\langle c_{f3}\rangle + \langle c_{f4}\rangle + \langle c_{f5}\rangle$.

Viscous dissipation contributes approximately 42.6% at $M_1 = 0.2$ and 42.8% at $M_2 = 0.7$, while turbulent dissipation accounts for approximately 46.1% at both Mach numbers. The contribution of the streamwise kinetic energy growth c_{f3} is approximately 11%, while the streamwise c_{f4} and spanwise c_{f5} heterogeneity components have a negligible impact of approximately 0.1% each. Viscous and turbulent dissipation do also dominate the skin friction in the actuated cases. However, for the viscous dissipation component c_{f1} a reduction of approximately 15.7% is observed in the CII case at $M_1 = 0.2$. At $M_2 = 0.7$, the reduction is more pronounced, with c_{f1} decreasing by 18.9% from 0.428 to 0.347. The turbulent dissipation component c_{f2} is substantially reduced, particularly in the CII case. At $M_1 = 0.2$, c_{f2} decreases by 21.4% from 0.461 in the reference case to 0.362. This reduction is even more significant at $M_2 = 0.7$, where c_{f2} is lowered by 47.1%. In the CII case at $M_2 = 0.7$, a significant shift is observed in the contributions from the streamwise kinetic energy growth c_{f3} and the streamwise heterogeneity c_{f4}. The negative value of c_{f3} describes an energy deficit, which is likely due to the suppression of quasistreamwise vortices. This suppression reduces the growth of kinetic energy in the streamwise direction. A similar energy deficit defined by negative c_f contributions was also observed by blowing actuation [44,45]. Simultaneously, there is a substantial increase in c_{f4} to 0.371. This indicates that the energy is redirected towards enhancing streamwise heterogeneity instead of contributing to streamwise kinetic growth. This redistribution means that at high Mach number conditions, particularly in the presence of a shock wave, the

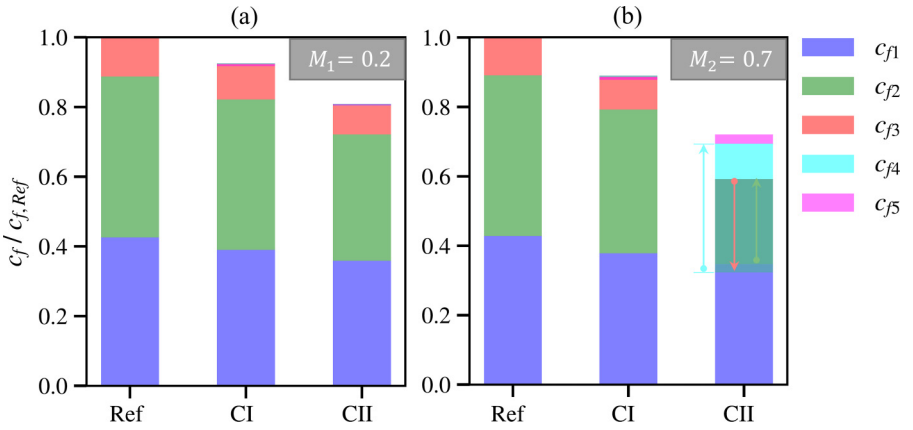


FIG. 13. Comparison of normalized skin-friction components c_{f1}, c_{f2}, c_{f3}, c_{f4}, and c_{f5}, expressed as a ratio of the total skin friction to the reference skin friction $c_f/c_{f,\mathrm{ref}}$, for several cases for (a) $M_1 = 0.2$ and (b) $M_2 = 0.7$. The color bars represent the contributions from viscous dissipation c_{f1} (blue), turbulent dissipation c_{f2} (green), streamwise kinetic energy growth c_{f3} (red), streamwise heterogeneity c_{f4} (cyan), and spanwise heterogeneity c_{f5} (magenta). The results are shown for the nonactuated reference cases (Ref) and the actuated cases (CI and CII). In (b), the arrows indicate the relative magnitude and sign of components. An arrow pointing upward (downward) denotes a positive (negative) contribution.

actuation induces significant nonuniformity in the flow. This nonuniformity is expressed in the increased c_{f4} since the flow becomes rather more heterogeneous than uniformly distributed in the streamwise direction. Interestingly, the combined value $c_{f3} + c_{f4}$ in CII at $M_2 = 0.7$ is very close to that of the reference case despite the vastly different underlying dynamics, particularly due to the negative contribution from c_{f3}. At $M_1 = 0.2$, however, the combined $c_{f3} + c_{f4}$ decreases progressively from 0.1115 in the reference case to 0.1014 in CI and further to 0.0829 in CII. This indicates a more homogeneous reduction in streamwise kinetic energy growth at the lower Mach number. The complex redistribution of energy components observed at higher Mach numbers, characterized by the negative contribution from c_{f3} and the pronounced increase in c_{f4}, does not occur at $M_1 = 0.2$. Finally, the spanwise heterogeneity component c_{f5} shows minimum variations across all cases. Only in CII at $M_2 = 0.7$ is a slight increase observed.

The spanwise shock wave formation process has a double impact on the skin friction components. While it significantly reduces the turbulent dissipation c_{f2} in the CII case at $M_2 = 0.7$, which results in a 47.1% reduction, it also increases the combined contributions of streamwise kinetic energy growth, streamwise heterogeneity, and spanwise heterogeneity ($c_{f3} + c_{f4} + c_{f5}$). This combined value rises to 0.1285 in the CII case, compared to 0.1089 in the reference case. This suggests that while the shock wave formation process reduces turbulent dissipation, it simultaneously enhances flow heterogeneity. Overall, the reduction in $c_{f1} + c_{f2}$ outweighs the increase in $c_{f3} + c_{f4} + c_{f5}$ and ensures a net decrease in skin friction despite the complex patterns introduced by the formation process of the shock wave.

IV. CONCLUSIONS

We presented a detailed analysis into drag reduction (DR) and net power saving (NPS) in turbulent boundary layers (TBLs), using spanwise traveling transversal waves (STTSW) at Mach numbers $M_1 = 0.2$ and $M_2 = 0.7$ at a fixed momentum based Reynolds number $\mathrm{Re}_\theta = 1000$.

The results reveal that higher drag reduction is achieved at higher Mach number, i.e., a maximum drag reduction of 19.2% at $M_1 = 0.2$ compared to 27.5% at $M_2 = 0.7$. The increased wave speed at $M_2 = 0.7$ induces spanwise shock waves and yields a more complex flow structure that is

summarized in a two-region wavelength-period drag-reduction map. In region I, which is characterized by lower wave speeds, the actuation yields positive net power saving, with only a marginal increase in drag reduction at a higher Mach number. Region II, however, which is defined by higher wave speeds, undergoes significant changes that result in a massive increase in drag reduction for greater Mach number and negative net power saving at M_2. For optimum drag reduction, the wave speed should be comparable to the free-stream velocity. When the Mach number increases, the optimum wave speed rises, which leads to the formation of spanwise shock waves, which massively lowers the friction drag. However, the higher drag reduction suffers from the higher negative net power savings.

A detailed analysis of the turbulence statistics shows that spanwise shock waves significantly modify near-wall turbulence by thickening the viscous sublayer and diminishing the logarithmic region. Furthermore, we concluded from the energy spectral analysis of $u'''u'''$ that quasistreamwise vortices are compressed in the streamwise direction (λ_x^+) and stretched in the spanwise direction (λ_z^+). These structural deformations lift the quasistreamwise vortices off the wall and reduce their direct interaction with the near-wall region, which results in drag reduction. In addition, the spectra of $v'''v'''$ and $w'''w'''$ show a more diffuse energy distribution and distinct structures that indicate that the formation of spanwise shock waves decomposes the large quasistreamwise vortices into smaller substructures. This process enhances energy diffusion, weakens vortex coherence, and reduces skin friction.

The modified Renard-Deck identity shows that viscous and turbulent dissipation are critical factors in drag reduction for both Mach numbers. The formation process of spanwise traveling waves significantly reduces turbulent dissipation. Reductions up to 21.4% at $M_1 = 0.2$ and 47.1% at $M_2 = 0.7$ are achieved. However, this process also introduces additional streamwise and spanwise heterogeneity, causing localized growth in skin friction. Nevertheless, the overall skin-friction reduction remains significant since the formation process of the spanwise shock waves enhances drag reduction by lowering the interaction of turbulent structures over most of the surface of the wave.

ACKNOWLEDGMENTS

The research was funded by the Deutsche Forschungsgemeinschaft (DFG) in the framework of the research projects SCHR 309/52 and SCHR 309/68. The authors gratefully acknowledge the Gauss Centre for Supercomputing e.V. [46] for funding this project by providing computing time on the GCS Supercomputer HAWK at Höchstleistungsrechenzentrum Stuttgart [47]. The first author expresses her sincere gratitude to the China Scholarship Council (CSC) for the financial support during her studies.

DATA AVAILABILITY

The data that support the findings of this article are not publicly available upon publication because it is not technically feasible and/or the cost of preparing, depositing, and hosting the data would be prohibitive within the terms of this research project. The data are available from the authors upon reasonable request.

[1] P. Ricco, M. Skote, and M. A. Leschziner, A review of turbulent skin-friction drag reduction by near-wall transverse forcing, Prog. Aerosp. Sci. **123**, 100713 (2021).

[2] H. Choi, P. Moin, and J. Kim, Active turbulence control for drag reduction in wall-bounded flows, J. Fluid Mech. **262**, 75 (1994).

[3] W.-J. Jung, N. Mangiavacchi, and R. Akhavan, Suppression of turbulence in wall-bounded flows by high-frequency spanwise oscillations, Phys. Fluids A **4**, 1605 (1992).
[4] Y. Du, V. Symeonidis, and G. Karniadakis, Drag reduction in wall-bounded turbulence via a transverse travelling wave, J. Fluid Mech. **457**, 1 (2002).
[5] M. Quadrio, P. Ricco, and C. Viotti, Streamwise-travelling waves of spanwise wall velocity for turbulent drag reduction, J. Fluid Mech. **627**, 161 (2009).
[6] I. Marusic, D. Chandran, A. Rouhi, M. K. Fu, D. Wine, B. Holloway, D. Chung, and A. J. Smits, An energy-efficient pathway to turbulent drag reduction, Nat. Commun. **12**, 5805 (2021).
[7] S. Klumpp, M. Meinke, and W. Schröder, Friction drag variation via spanwise transversal surface waves, Flow Turb. Combust. **87**, 33 (2011).
[8] N. Tomiyama and K. Fukagata, Direct numerical simulation of drag reduction in a turbulent channel flow using spanwise traveling wave-like wall deformation, Phys. Fluids **25**, 105115 (2013).
[9] M. Albers, P. S. Meysonnat, D. Fernex, R. Semaan, B. R. Noack, and W. Schröder, Drag reduction and energy saving by spanwise traveling transversal surface waves for flat plate flow, Flow Turbul. Combust. **105**, 125 (2020).
[10] M. Albers and W. Schröder, Lower drag and higher lift for turbulent airfoil flow by moving surfaces, Int. J. Heat Fluid Flow **88**, 108770 (2021).
[11] E. Mäteling, M. Albers, and W. Schröder, How spanwise travelling transversal surface waves change the near-wall flow, J. Fluid Mech. **957**, A30 (2023).
[12] K. Fukagata, K. Iwamoto, and Y. Hasegawa, Turbulent drag reduction by streamwise traveling waves of wall-normal forcing, Annu. Rev. Fluid Mech. **56**, 69 (2024).
[13] E. Lagemann, M. Albers, C. Lagemann, and W. Schröder, Impact of Reynolds number on the drag reduction mechanism of spanwise travelling surface waves, Flow Turbul. Combust. **113**, 27 (2024).
[14] J. Yao and F. Hussain, Supersonic turbulent boundary layer drag control using spanwise wall oscillation, J. Fluid Mech. **880**, 388 (2019).
[15] M. Ruby and H. Foysi, Active control of compressible channel flow up to $Ma_b = 3$ using direct numerical simulations with spanwise velocity modulation at the walls, GAMM-Mitteilungen **45**, e202200004 (2022).
[16] F. Gattere, M. Zanolini, D. Gatti, M. Bernardini, and M. Quadrio, Turbulent drag reduction with streamwise-travelling waves in the compressible regime, J. Fluid Mech. **987**, A30 (2024).
[17] Institute of Aerodynamics, RWTH Aachen University, m-AIA multiphysics flow solver in Aachen, Zenodo (2024), doi: 10.5281/zenodo.13350586.
[18] M.-S. Liou and C. J. Steffen, Jr., A new flux splitting scheme, J. Comput. Phys. **107**, 23 (1993).
[19] M. Meinke, W. Schröder, E. Krause, and T. Rister, A comparison of second-and sixth-order methods for large-eddy simulations, Comput. Fluids **31**, 695 (2002).
[20] C. W. Hirt, A. A. Amsden, and J. Cook, An arbitrary lagrangian-eulerian computing method for all flow speeds, J. Comput. Phys. **14**, 227 (1974).
[21] B. Roidl, M. Meinke, and W. Schröder, A zonal RANS-LES method for compressible flows, Comput. Fluids **67**, 1 (2012).
[22] B. Roidl, M. Meinke, and W. Schröder, Numerical investigation of shock wave boundary-layer interaction using a zonal RANS-LES ansatz, in *High Performance Computing in Science and Engineering'10: Transactions of the High Performance Computing Center, Stuttgart (HLRS) 2010* (Springer, Berlin, 2011), pp. 369–383.
[23] M. Albers, X. Shao, and W. Schröder, Energy efficient actuated drag reduced compressible turbulent flat plate flow, Int. J. Heat Fluid Flow **106**, 109314 (2024).
[24] F. Gattere, A. Chiarini, E. Gallorini, and M. Quadrio, Structure function tensor equations with triple decomposition, J. Fluid Mech. **960**, A7 (2023).
[25] P. Huang, G. N. Coleman, and P. Bradshaw, Compressible turbulent channel flows: DNS results and modelling, J. Fluid Mech. **305**, 185 (1995).
[26] D. Gatti and M. Quadrio, Reynolds-number dependence of turbulent skin-friction drag reduction induced by spanwise forcing, J. Fluid Mech. **802**, 553 (2016).

[27] T. A. Oliver, N. Malaya, R. Ulerich, and R. D. Moser, Estimating uncertainties in statistics computed from direct numerical simulation, Phys. Fluids **26**, 035101 (2014).
[28] J. Jeong and F. Hussain, On the identification of a vortex, J. Fluid Mech. **285**, 69 (1995).
[29] A. G. Kravchenko, H. Choi, and P. Moin, On the relation of near-wall streamwise vortices to wall skin friction in turbulent boundary layers, Phys. Fluids A **5**, 3307 (1993).
[30] K.-S. Choi, Near-wall structure of a turbulent boundary layer with riblets, J. Fluid Mech. **208**, 417 (1989).
[31] K.-S. Choi, A survey of the turbulent drag reduction using passive devices, NASA STI/Recon Technical Report N **85**, 20268 (1984).
[32] A. Lozano-Durán and J. Jiménez, Effect of the computational domain on direct simulations of turbulent channels up to $\mathrm{Re}_\tau = 4200$, Phys. Fluids **26**, 011702 (2014).
[33] C. Smith and S. Metzler, The characteristics of low-speed streaks in the near-wall region of a turbulent boundary layer, J. Fluid Mech. **129**, 27 (1983).
[34] C. Wenzel, T. Gibis, and M. Kloker, About the influences of compressibility, heat transfer and pressure gradients in compressible turbulent boundary layers, J. Fluid Mech. **930**, A1 (2022).
[35] K. Fukagata, K. Iwamoto, and N. Kasagi, Contribution of Reynolds stress distribution to the skin friction in wall-bounded flows, Phys. Fluids **14**, L73 (2002).
[36] N. Renard and S. Deck, A theoretical decomposition of mean skin friction generation into physical phenomena across the boundary layer, J. Fluid Mech. **790**, 339 (2016).
[37] M. de Giovanetti, Y. Hwang, and H. Choi, Skin-friction generation by attached eddies in turbulent channel flow, J. Fluid Mech. **808**, 511 (2016).
[38] Y. Kametani, K. Fukagata, R. Örlü, and P. Schlatter, Effect of uniform blowing/suction in a turbulent boundary layer at moderate Reynolds number, Int. J. Heat Fluid Flow **55**, 132 (2015).
[39] Y. Fan, W. Li, and S. Pirozzoli, Decomposition of the mean friction drag in zero-pressure-gradient turbulent boundary layers, Phys. Fluids **31**, 086105 (2019).
[40] Y. Fan, W. Li, M. Atzori, R. Pozuelo, P. Schlatter, and R. Vinuesa, Decomposition of the mean friction drag in adverse-pressure-gradient turbulent boundary layers, Phys. Rev. Fluids **5**, 114608 (2020).
[41] P. Ricco and M. Skote, Integral relations for the skin-friction coefficient of canonical flows, J. Fluid Mech. **943**, A50 (2022).
[42] W. Li, Y. Fan, D. Modesti, and C. Cheng, Decomposition of the mean skin-friction drag in compressible turbulent channel flows, J. Fluid Mech. **875**, 101 (2019).
[43] A. Smits, N. Matheson, and P. Joubert, Low-Reynolds-number turbulent boundary layers in zero and favorable pressure gradients, J. Ship Res. **27**, 147 (1983).
[44] Y. Fan, M. Atzori, R. Vinuesa, D. Gatti, P. Schlatter, and W. Li, Decomposition of the mean friction drag on an naca4412 airfoil under uniform blowing/suction, J. Fluid Mech. **932**, A31 (2022).
[45] R. Ma, Z. Gao, L. Lu, and S. Chen, Skin-friction drag reduction by local porous uniform blowing in spatially developing compressible turbulent boundary layers, Phys. Fluids **34**, 125130 (2022).
[46] http://www.gauss-centre.eu
[47] http://www.hlrs.de